




# A *Chandra* X-Ray and Infrared Study of the Stellar Population in the High-mass Star-forming Region IRAS 16562-3959

Virginie A. Montes<sup>1</sup> , Peter Hofner<sup>1,2</sup>, Lidia M. Oskinova<sup>3</sup>, and Hendrik Linz<sup>4</sup>

<sup>1</sup> Physics Department, New Mexico Institute of Mining and Technology, 801 Leroy Place, Socorro, NM 87801, USA; [virginie.montes@student.nmt.edu](mailto:virginie.montes@student.nmt.edu)

<sup>2</sup> Adjunct Astronomer at the National Radio Astronomy Observatory, Charlottesville, VA, USA

<sup>3</sup> Institute for Physics and Astronomy, University of Potsdam, D-14476 Potsdam, Germany

<sup>4</sup> Max-Planck-Institute for Astronomy, Königstuhl 17, D-69117 Heidelberg, Germany

Received 2018 June 17; revised 2019 November 6; accepted 2019 November 19; published 2020 January 15

## Abstract

We present the results from *Chandra* X-ray observations, and near- and mid-infrared analysis, using VISTA/VVV and *Spitzer*/GLIMPSE catalogs, of the high-mass star-forming region IRAS 16562-3959, which contains a candidate for a high-mass protostar. We detected 249 X-ray sources within the ACIS-I field of view. The majority of the X-ray sources have low count rates ( $<0.638$  cts/ks) and hard X-ray spectra. The search for YSOs in the region using VISTA/VVV and *Spitzer*/GLIMPSE catalogs resulted in a total of 636 YSOs, with 74 Class I and 562 Class II YSOs. The search for near- and mid-infrared counterparts of the X-ray sources led to a total of 165 VISTA/VVV counterparts, and a total of 151 *Spitzer*/GLIMPSE counterparts. The infrared analysis of the X-ray counterparts allowed us to identify an extra 91 Class III YSOs associated with the region. We conclude that a total of 727 YSOs are associated with the region, with 74 Class I, 562 Class II, and 91 Class III YSOs. We also found that the region is composed of 16 subclusters. In the vicinity of the high-mass protostar, the stellar distribution has a core-halo structure. The subcluster containing the high-mass protostar is the densest and the youngest in the region, and the high-mass protostar is located at its center. The YSOs in this cluster appear to be substantially older than the high-mass protostar.

*Unified Astronomy Thesaurus concepts:* Young star clusters (1833); Massive stars (732); Protostars (1302); Pre-main sequence stars (1290); Star formation (1569); X-ray stars (1823)

*Supporting material:* machine-readable tables

## 1. Introduction

High-mass stars play a dominant role in the physical, chemical, and morphological structure of their host galaxies (e.g., Kennicutt 1998; Cesaroni et al. 2005), but despite their importance, the formation and early evolution of high-mass stars is still not well understood. The two main theories trying to explain high-mass star formation are the monolithic core accretion model (McKee & Tan 2003) and the competitive accretion model (Bonnell et al. 2001). In the monolithic core accretion model, the physical properties of the molecular core determines the final mass of the star, and it will form in isolation, or in small-N multiple systems. In contrast, in the competitive accretion model, the high-mass star forms at the center of a low-mass stellar cluster, and the mass of the high-mass star is related to the properties of the cluster. See the recent review of Tan et al. (2014) for more details. Characterizing the stellar population associated with high-mass star formation is thus crucial for deciding between the two main theories. Studies of more evolved stellar systems indicate that most high-mass stars are in fact formed in a dense cluster environment (Lada & Lada 2003), but there is a small population of high-mass stars that appear to have formed in isolation (de Wit et al. 2005; Oskinova et al. 2013). As dynamical evolution can significantly change the appearance of a young stellar system, studying early stages of high-mass star formation in young, and hence embedded regions is critical.

Many previous studies of high-mass star-forming regions have been carried out at infrared wavelengths (e.g., Lada & Lada 2003) because long wavelengths can penetrate the dust efficiently. However, observing only at infrared wavelengths

prevents the detection of YSOs that have partially, or completely lost their circumstellar disk. The *Chandra* X-ray Observatory allows an alternative view of young stellar populations, as X-ray extinction is low at energies above a few keV, and the background/foreground contamination is relatively small, mainly from nearby stars and active galactic nuclei (AGNs). Furthermore, Classical T Tauri Stars (CTTS) and weak-line T Tauri Stars (WTTS) are bright in X-rays (Feigelson & Montmerle 1999), and earlier evolutionary phases of YSOs (Class I) are also well known X-ray emitters (Grosso et al. 1997; Neuhäuser & Preibisch 1997). Thus, combining X-ray data with infrared data is an efficient way to study the stellar population in regions where massive stars are forming. In this paper, we present such a study for the high-mass star-forming region IRAS 16562-3959, where we have combined *Chandra* X-ray images and spectra with near- and mid-infrared data from the VISTA/VVV survey, and the *Spitzer* GLIMPSE survey.

The high-mass protostellar candidate G345.4938+01.4677 associated with IRAS 16562-3959 is located at the northern end of the Sco OB1 association (e.g., Damiani 2018). At a distance of 1.7 kpc the FIR luminosity of the IRAS source is  $L = 7 \times 10^4 L_{\odot}$ , clearly indicating the presence of high-mass (proto) stars (López et al. 2011). Guzmán et al. (2010) discovered this source at 6 cm with ATCA, while searching for ionized jets in regions of high-FIR luminosity. The 6 cm ATCA data show five aligned continuum sources, where the bright central source presumably indicates the position of the high-mass protostar. The four symmetrically displaced sources have been observed to move away from the central source at high speed (Guzmán et al. 2014), and are likely due to shock

**Table 1**  
Log of Observations

Obs #	Chandra Cycle	ID	Instrument	Exposure	Date	Roll Angle
1	14	ObsID 14537	ACIS-I	5.02 ks	2013 Feb 2	95°45
2	16	ObsID 16658	ACIS-I	38.58 ks	2015 Jun 30	300°22
3	16	ObsID 17691	ACIS-I	40.07 ks	2015 Jul 3	300°22

ionization from fast outflowing matter in a jet. IRAS 16562-3959 is also associated with a slower ionized wind, an infalling envelope, and a bipolar molecular outflow, and the mass of the central object has been estimated as  $\sim 15 M_{\odot}$  (Guzmán et al. 2014). Recently, López-Calderon et al. (2016) reported  $^{13}\text{CO}(3-2)$  APEX observations of this region, which showed that the high-mass protostellar candidate is located at the column density maximum, further demonstrating its youth.

It is important to point out that while many similar studies have been performed in high-mass star-forming regions (e.g., M17, W3, see e.g., Hofner et al. 2002; Townsley et al. 2014) where H II regions clearly indicate the presence of fully formed massive stars, the IRAS 16562-3959 region contains only a weak radio source, which is clearly in a pre-H II region phase of evolution, and is also the only manifestation of high-mass star formation within 2 pc. It thus allows us to study the stellar population associated with the formation of a high-mass star in a very early evolutionary phase.

In Section 2, we describe the *Chandra* observations and data reduction of the region. In Section 3, the X-ray results and analysis of the region are described. A near- and mid-infrared analysis of the region is presented in Section 4. X-ray and infrared source associations are discussed in Section 5. In Section 6, we present a subcluster analysis of the large-scale region. In Section 7, we discuss the observational results, and in Section 8 we summarize our general conclusions.

## 2. Chandra X-Ray Observations and Data Reduction

The IRAS 16562-3959 high-mass star-forming region was observed with the *Chandra X-Ray Observatory* at three different epochs detailed in Table 1. The first observation (Obs# 1) was made in cycle 14 with an exposure time of 5.02 ks, and the second (Obs# 2) and third observations (Obs# 3) were obtained in cycle 16 with exposure times of 38.58 ks and 40.07 ks, respectively, corresponding to a total exposure time of 83.67 ks, i.e., approximately 23 hr. No background flares were detected during these three epochs. The observations were carried out using the imaging array of the Advanced CCD Imaging Spectrometer camera (ACIS-I). ACIS-I consists of four  $1024 \times 1024$  pixel color-color diagrams (CCDs) covering a field of view of  $17' \times 17'$ , and has an energy range from 0.1 to 10 keV. For details on the instrument see Weisskopf et al. (1996, 2002) and Garmire et al. (2003). The nominal pointing position used for the three observations was R.A.(J2000) =  $16^{\text{h}}59^{\text{m}}41^{\text{s}}.60$ , decl. (J2000) =  $-40^{\circ}03'43''.6$ , which are the coordinates of the high-mass protostar (Guzmán et al. 2010). The satellite roll angle (i.e., the angle between the celestial north and the Z-axis of the spacecraft) for Obs# 1 was 95°45 and 300°22 for Obs# 2 and 3.

Data reduction was performed using the CIAO software package version 4.7 and CALDB 4.6.8 provided by the *Chandra* X-ray Center. The data were recalibrated using the *chandra\_repro* reprocessing script to create a new level = 2 event file and a new bad pixel file for each observation. Before any analysis, it is necessary to correct the absolute astrometry

on the three observations. For this, we first used the Obs# 2 data to match *Chandra* sources with NIR sources from the 2MASS catalog. A set of 23 bright sources were selected in the center of the field of view of the ACIS-I array and compared to their 2MASS counterparts. A systematic offset of  $0''.1$  toward the south and  $0''.35$  toward the west was observed. After astrometry correction, the rms offset between *Chandra* Obs# 2 and 2MASS sources was about  $0''.1$ . Subsequently, we corrected the astrometry of Obs# 1 and 3 to match the position of the 23 X-ray sources (when detected) of Obs# 2.

Finally, we filtered the data in three different energy ranges: 0.5–2 keV (soft band), 2–8 keV (hard band), and 0.5–8 keV (full band) and created flux images, exposure maps, and PSF maps for each observation and each energy range.

## 3. X-Ray Results and Analysis

### 3.1. Detection

The source identification in the ACIS-I field of view was performed using *wavdetect*, a wavelet-based source detection algorithm (Freeman et al. 2002), in three energy ranges: 0.5–2 keV (soft band), 2–8 keV (hard band), and 0.5–8 keV (full band). We used a threshold significance of  $10^{-6}$  corresponding to one spurious source in the field of view of ACIS-I, and wavelet scale sizes from 1 to 16 pixels incremented by a factor  $\sqrt{2}$ . The search was done separately in the three observations and the source lists were joined. Sources with at least 5 counts in the combined observations were considered to be real sources. We note that this detection limit is rather conservative, and clearly leads to a lower limit for the number of detected source (e.g., Damiani 2018). Due to the large variation of the extinction in the region (our spectral fits imply a range of  $N_H$  between  $2 \times 10^{21}$  and  $5 \times 10^{23} \text{ cm}^{-2}$ ; see below), this detection limit corresponds to a range of limiting luminosities of  $L_{X,\text{lim}} = 2.5 \times 10^{29} - 1.6 \times 10^{32} \text{ erg s}^{-1}$ , for a thermal plasma with  $kT = 1 \text{ keV}$ .

A total of 249 sources were detected in the field of view for the full energy range in the combined three observations, as shown in the flux image in Figure 1. In Obs# 1, a total of 38 sources were detected in the full band, we found 19 sources in the soft band and 20 sources in the hard band. In Obs# 2, a total of 208 sources were detected in the full range of energy, with 102 sources for the soft band and 147 sources for the hard band. In Obs# 3, a total of 198 sources were detected in the full band, 106 sources were detected in the soft band, and 148 sources were detected in the hard band. In Table 2 we list the observed X-ray properties of all our detections. Column (1) lists the source number, column (2) and (3) give the *Chandra* positions, column (4) is the observed count rate, and column (5) shows the observed X-ray flux. In column (6) we list the hardness ratio for each source defined as  $\text{HR} = \frac{h_x - s_x}{h_x + s_x}$ , where  $h_x$  is the count rate in the 2–8 keV energy range, and  $s_x$  is the count rate in the 0.5–2 keV energy range. In column (7) we give the short-term variability for each source in each

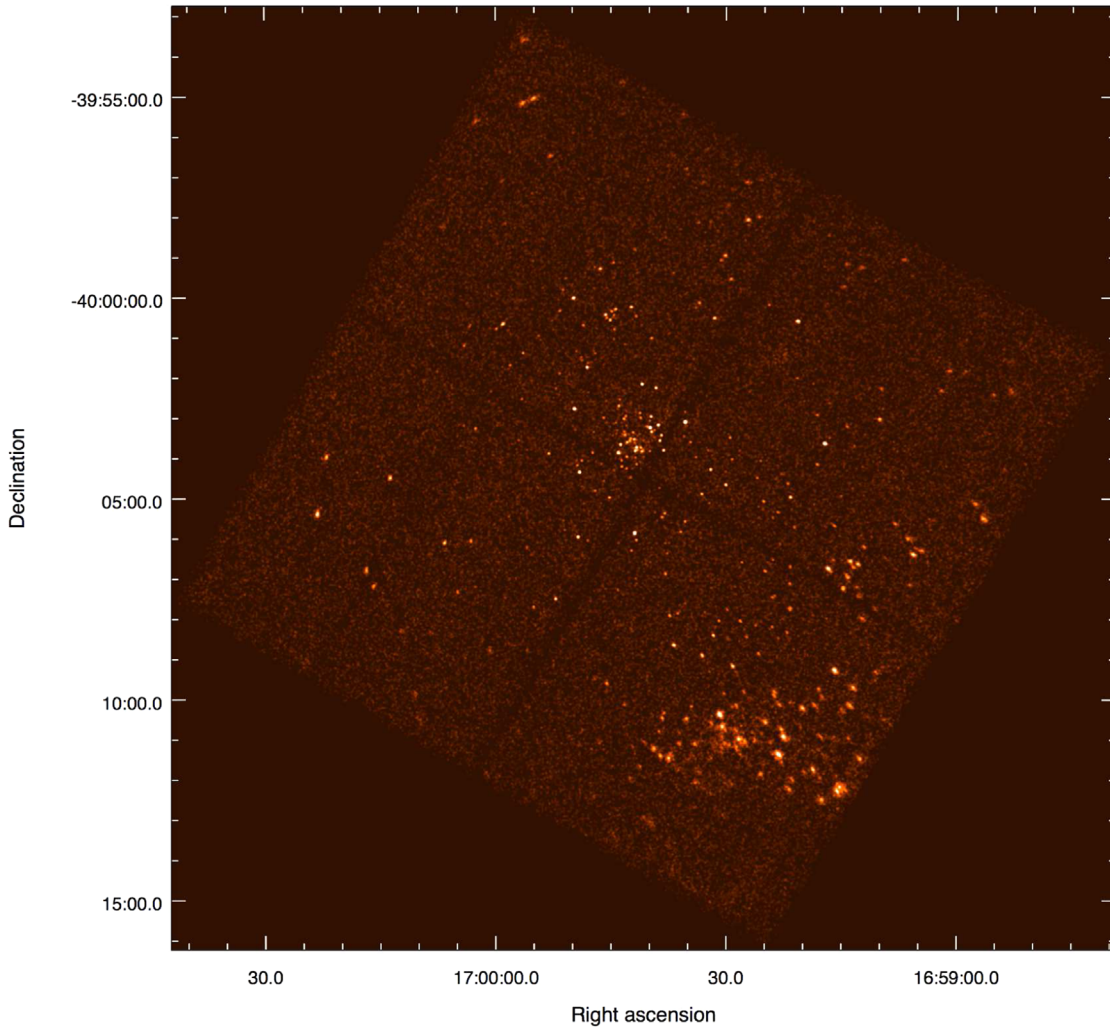


**Figure 1.** Color image of the three combined observations for the full  $17' \times 17'$  ACIS-I field in the 0.5–8 keV band toward IRAS16562-3959. A total of 249 X-ray point sources were detected.

**Table 2**  
X-Ray Sources

Source #	R.A. (J2000)	Decl. (J2000)	Count Rate (cts ks <sup>-1</sup> )	$F_x$ $10^{-14}$ (erg cm <sup>-2</sup> s <sup>-1</sup> )	HR	S.T. Var. Index Obs #	L. T. Var. Parameter	Var.
(1)	(2)	(3)	(4)	(5)	(6)	1/2/3 (7)	(8)	(9)
1	16 58 52.73	−40 02 18.2	0.77	1.28	0.69	.../6/0	1.49	STV
2	16 58 55.13	−40 02 25.4	0.39	0.70	0.75	.../1/...	...	...
3	16 58 56.35	−40 05 30.6	1.75	1.53	−0.31	.../0/0	2.77	...
4	16 58 57.47	−40 05 07.6	0.98	2.57	0.65	.../1/0	0.96	...
5	16 59 01.03	−40 01 50.1	0.44	0.56	−0.77	.../1/...	...	...

(This table is available in its entirety in machine-readable form.)

observation, column (8) shows the long-term variability of each source, and column (9) lists for each source whether it is variable and which type of variability it shows. Source variability will be discussed in Section 3.2. As expected by studies of stellar X-ray emission in highly embedded clusters at kiloparsec distances, most sources are fairly faint, with approximately 70% of the sources having less than 50 counts (count rate 0.638 cts/ks), and according to our hardness ratio

classification, the majority of sources have a relatively hard observed X-ray spectrum.

### 3.2. Timing Analysis and Source Variability

As we have observed this star-forming region at three different epochs, we want to determine if the sources in the field exhibit short-term and/or long-term variabilities. We will



refer to changes in count rate of a source within one observation as short-term variability. On the other hand, long-term variability corresponds to the overall change in count rate of a source between observations. A number of physical mechanisms, which could explain the different types of variability have been discussed in Flaccomio et al. (2012).

To determine if the sources display short-term variability, we first apply the barycenter correction to each observation. Then we compute the fractional area of each source, which creates a correction for instrumental effects, needed for input to the *glvary* tool. Subsequently, we ran *glvary* for each individual source, on each observation subdivided into temporal bins of approximate width 2 ks. The *glvary* script uses the Gregory–Loredo variability test algorithm (Gregory & Loredo 1992) which is insensitive to the light-curve shape and does not overinterpret data in low count rate sources like the Kolmogorov–Smirnov (K-S) test can do.<sup>5</sup> This test gives us a variability index indicating if the source is variable or not as shown in Table 2 column 7. If the variability index (S.T. Var) is between 0 and 3, it is unlikely that the source is variable. If S.T. Var is 4 or 5, the source may be variable, and if S.T. Var is above 5, the source is definitely variable (Rots 2006).

To determine if the sources have long-term variability, we follow the method from Fridriksson et al. (2008) by computing a significance parameter  $S$  (L. T. Var. parameter) for long-term flux variability for each source:

$$S = \frac{|F_{\max} - F_{\min}|}{\sqrt{\sigma_{F_{\max}}^2 + \sigma_{F_{\min}}^2}}, \quad (1)$$

where  $F_{\max}$  and  $F_{\min}$  are the maximum and minimum X-ray count rates during the three observations for each source, and  $\sigma_{F_{\max}}$  and  $\sigma_{F_{\min}}$  are the corresponding errors. A source is defined as long-term variable if  $S > 3$ . The long-term variability parameter for each source is listed in Table 2 column (8). In Figure 2, we show a sample of sources exhibiting short-term and/or long-term variability.

### 3.3. Spectroscopy

A spectrum for each source and for each observation was extracted with *srcflux*. To get a single spectrum for each source for all observations, the coadding of the spectra and response files was done using *combine\_spectra*. The fitting of each coadded spectrum was then run using Sherpa v1. We used an Absorption $\times$ 1-Temperature model using the *xswabs* and *xspecc* models, with an abundance frozen to 0.3 solar abundance in all cases, which is typical for YSOs (Imanishi et al. 2001). Due to the weakness of the sources, we were only able to obtain meaningful fit results for 98 sources, using the following method: after a first initial simultaneous fitting of  $N_H$ ,  $T$  and emission measure (EM), we kept the fit results if the uncertainties for the parameters were reasonable. This was the case for six sources only. If the best-model fit showed large uncertainty for the fitted parameters, we froze the fitted value for  $T$  and redid the fit. This was the case for 88 sources. In 4 cases the value for the temperature resulted initially in unreasonable high values, and in these cases we assumed and froze a value for  $T$ , and fitted for the other parameters. The temperature for source # 8 was frozen at 2.51 keV, at 0.50 keV for sources # 15 and 23, and at 1.10 keV for source # 39. All

the fitting results are listed in Table 3, and sample spectra are shown in Figure 3.

## 4. Infrared Analysis of the Region

In order to carry out a more complete analysis of the evolution of the YSO population in the region, we added to our set of X-ray data, all infrared sources detected within a distance of 15' from the high-mass protostar, using mid-infrared ([3.6], [4.5], [5.8], and [8.0]  $\mu\text{m}$ ) data from the *Spitzer*/GLIMPSE<sup>6</sup> (Benjamin et al. 2003) and near-infrared ( $J$ ,  $H$ , and  $K_s$  bands) VISTA/VVV<sup>7</sup> (Minniti et al. 2010) surveys. A total of 17422 mid-infrared sources were found in the *Spitzer*/GLIMPSE catalog, and 136183 near-infrared sources were found in the VISTA/VVV catalog. This set of data in principle allows us to identify YSOs with disks (Class I and Class II).

To determine foreground and background contamination by star-forming galaxies, AGNs, shock emission, and extended PAH emission, as well as field stars, we performed the infrared color selection method described in Gutermuth et al. (2009). In Phase I of this method, we used only GLIMPSE sources that have photometry in all four IRAC bands, and have photometric uncertainties  $\sigma < 0.2$  mag in all four bands, which corresponds to a total of 2723 sources. In Figure 4 we show CCDs from the first step of the Phase I selection method, that allowed us to identify contamination from star-forming galaxies and AGNs. Then, we proceeded to the elimination of shock emission and extended PAH emission contamination, as well as YSO class selection as shown on Figure 5. This procedure resulted in a total of 2702 *Spitzer*/GLIMPSE sources without contamination. We obtained a total of 42 sources classified as Class I, and 177 sources classified as Class II. We continued with a process similar to the Phase II selection method described by Gutermuth et al. (2009), which we slightly modified due to the use of VISTA/VVV data instead of 2MASS data used in the Gutermuth et al. (2009) paper. In this step, both *Spitzer*/GLIMPSE and VISTA/VVV data were used. Specifically, the Phase II selection method is applied to *Spitzer*/GLIMPSE sources that lack [5.8] and/or [8.0] detections. The *Spitzer*/GLIMPSE sources were first matched with their VISTA/VVV counterparts. We only selected high-quality VISTA/VVV detections with  $\sigma < 0.1$  mag, and *Spitzer*/GLIMPSE detections with photometric uncertainties  $\sigma < 0.2$  mag in the detected bands for this analysis. A cross-match of both catalogs was done using a search radius of 1'', to create a matched list of 13,309 sources. A further selection on these sources was done using their VISTA/VVV magnitudes. We excluded stars with saturated photometry (Soto et al. 2013), by limiting the magnitudes of the detected VISTA/VVV sources to 13.8, 12.8, and 12.8, for the  $J$ ,  $H$ , and  $K_s$  bands, respectively. A total of 9974 non-saturated sources were selected. Whenever possible we checked for contamination using similar color-color criteria as described for Phase I in Gutermuth et al. (2009), and ended up with a total of 9844 sources without contamination. We selected this sample of 9844 stars where objects with infrared excesses are expected to be found. To select these infrared excess sources, we used the dereddened color selection criteria detailed in Gutermuth et al. (2009) with  $[K-[3.6]]_0$  and  $[[3.6]-[4.5]]_0$  colors. Displaying the position of all the new infrared excess candidates showed that they are

<sup>5</sup> CIAO manual.

<sup>6</sup> <http://irsa.ipac.caltech.edu/>

<sup>7</sup> <http://horus.roe.ac.uk/vsa/>



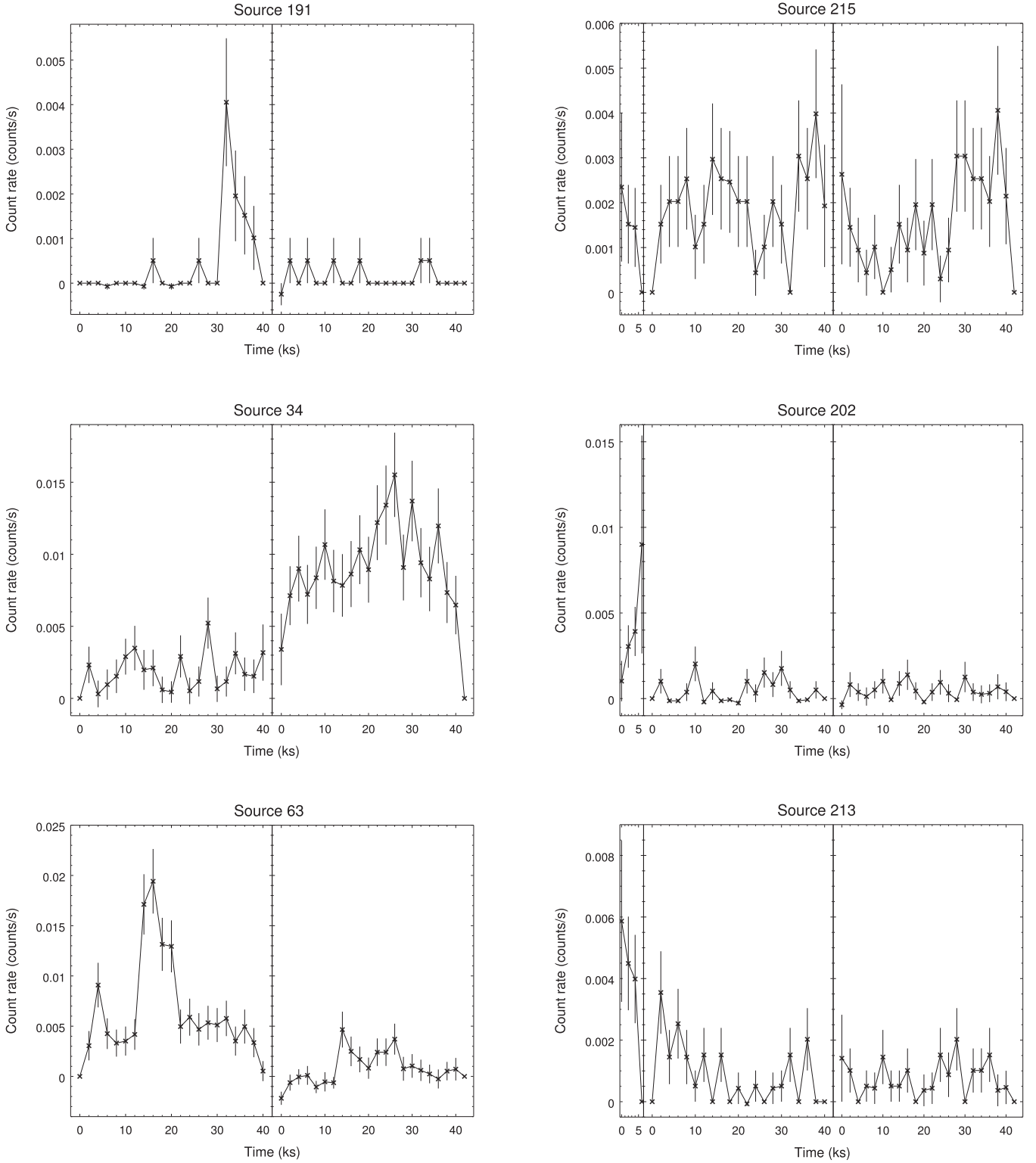


**Figure 2.** Sample light curves of sources exhibiting short-term and/or long-term variability. The three observations are plotted next to each other. Note that sources on the left panel were not detected in Obs #1, hence we are only showing the light curves corresponding to Obs #2 and 3. Sources #191 and 215 exhibit short-term variability. For source #191, a flare is observed at the end of Obs #2. Sources #34 and 202 exhibit long-term variability, with markedly increased X-ray activity during Obs #3 for source #34, and in Obs #1 for source #202. Sources #63 and 213 exhibit both short-term and long-term variability. Source #63 shows possible flares in both observations and a higher base X-ray activity in Obs #2. Source #213 shows a short-term variability during Obs #2 and a higher X-ray emission level in Obs #1.

uniformly distributed in the region, thus we consider that our selected data set might still suffer contamination by foreground sources. To eliminate any possible chance of selecting any contaminant, we therefore applied additional selection criteria

to these infrared excess sources candidates, as described in Winston et al. (2011) and Megeath et al. (2012), by plotting two CCDs, as shown in Figure 6. The first selection was done using the CCD  $J-H$  versus  $H-[4.5]$ , with the slope of the

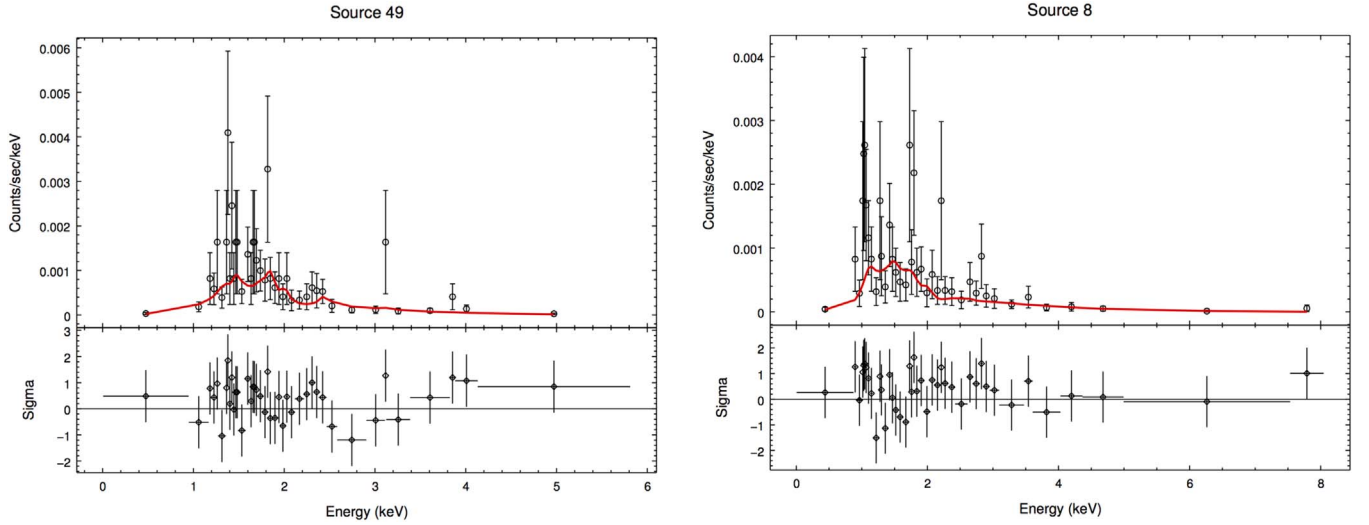


**Figure 3.** Sample spectra as described in the text. For source #49 we were able to obtain a simultaneous fit of  $N_H$ ,  $T$ , and emission measure, whereas for Source #8 the temperature was frozen in the fit.

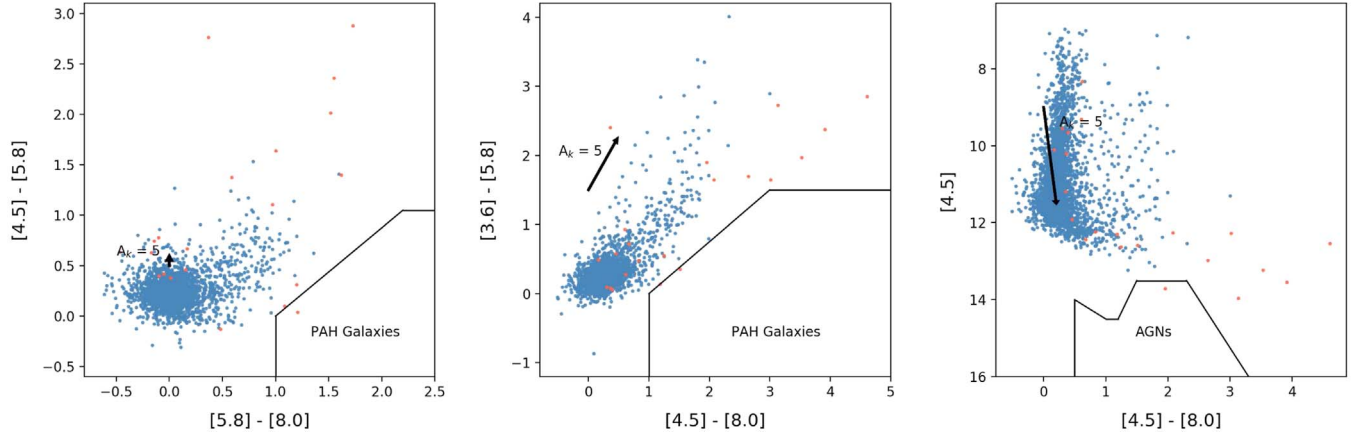


**Figure 4.** Color-color diagrams (CCDs) used for the determination of the contamination due to star-forming galaxies (left and middle panels); and AGNs (right panel); see Gutermuth et al. (2009) for more details. Orange dots correspond to all contamination found in Phase I; blue dots are field stars.

**Table 3**  
X-Ray Properties

Source #	$N_H$ $10^{22} \text{ (cm}^{-2}\text{)}$	kT (keV)	EM $10^{-5} \text{ (cm}^{-3}\text{)}$	$F_{x,c}$ $10^{-14} \text{ (erg cm}^{-2} \text{ s}^{-1}\text{)}$	$\log L_{x,c}$ ( $\text{erg s}^{-1}$ )	Reduced $\chi^2$
(1)	(2)	(3)	(4)	(5)	(6)	(7)
3	$1.07^{+0.28}_{-0.23}$	0.78	$10.58^{+3.52}_{-2.93}$	$11.93^{+3.42}_{-3.37}$	31.62	0.60
7	$1.38^{+0.88}_{-0.58}$	1.23	$3.09^{+2.21}_{-1.48}$	$2.93^{+1.90}_{-1.72}$	31.01	0.64
8	$0.42^{+0.42}_{-0.31}$	$2.51^a$	$2.31^{+0.90}_{-0.72}$	$2.45^{+0.84}_{-0.77}$	30.93	0.73
10	$2.47^{+1.37}_{-0.89}$	2.52	$3.18^{+1.48}_{-1.23}$	$3.34^{+1.45}_{-1.46}$	31.06	0.74
12	$3.81^{+1.78}_{-1.35}$	1.09	$9.08^{+6.97}_{-5.09}$	$9.30^{+6.25}_{-5.94}$	31.51	0.43

**Note.**

<sup>a</sup> The temperature was assumed and frozen for these sources.

(This table is available in its entirety in machine-readable form.)

reddening band  $\frac{E_{J-H}}{E_H - [4.5]} = 0.96$  (Chen et al. 2013). The second color selection was done using the CCD  $H-K_S$  versus  $K_S - [4.5]$  with the slope of the reddening band  $\frac{E_H - K_S}{E_{K_S - [4.5]}} = 0.98$  (Chen et al. 2013). We defined as YSOs all sources passing the selection criteria of the first or of the second CCD, and found a

total of 1566 YSOs. Initial inspection of this selection indicated that there was still contamination by normally reddened stars, and the limits were moved by 0.2 mag toward the red compared with the formulas given by Winston et al. (2007) and Jose et al. (2016). To then isolate Class I and Class II YSOs from these sources, we used the Phase II color selection from

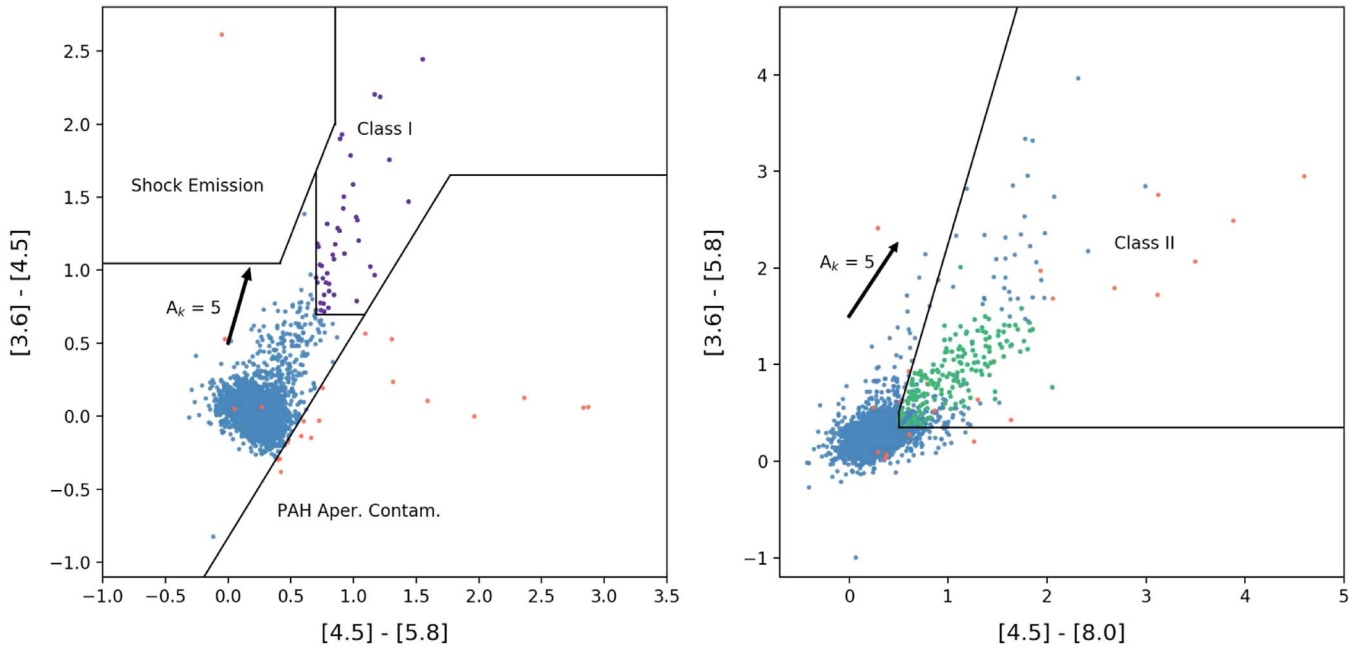


**Figure 5.** CCDs used to determine contamination and classification of sources. The left panel shows the criteria to isolate unresolved shock emission knots and sources with PAH aperture contamination, and also defines Class I protostars (purple dots). The right panel shows the location of Class II YSOs (green dots). Orange dots correspond to all contamination found in Phase I; blue dots are field stars.

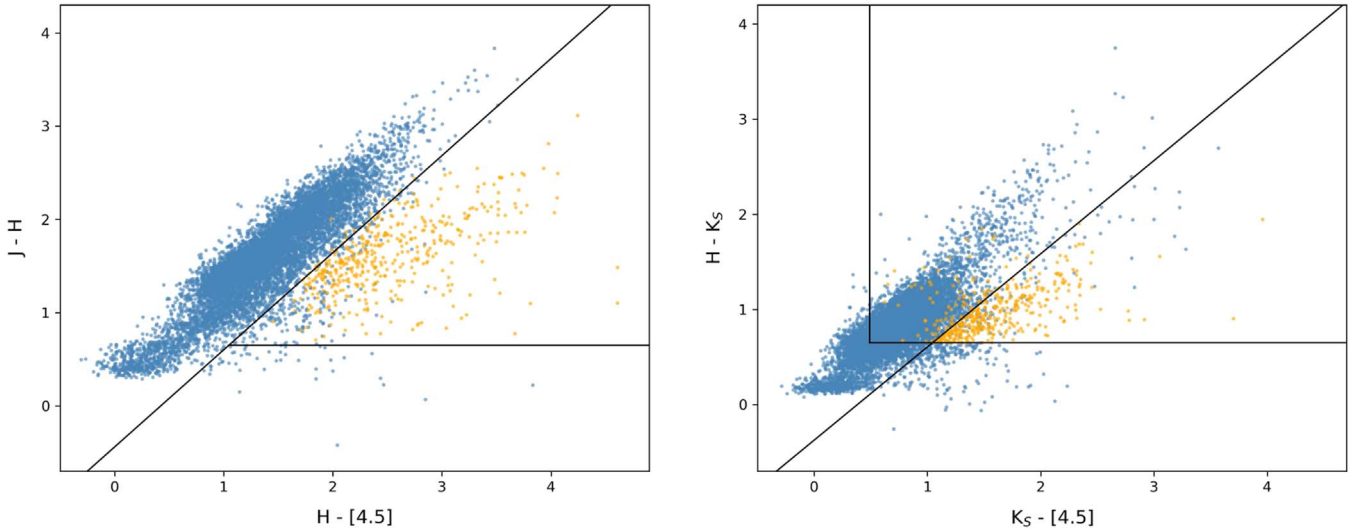


**Figure 6.** CCDs showing the infrared excess selection. The orange dots correspond to the infrared excess sources, and the blue dots correspond to field stars. Left: CCD  $J-H$  vs.  $H-[4.5]$ . The black lines mark the limit for the infrared selection with  $(J-H) < [(H-[4.5])-1.0]/0.96 + 0.6$  (Winston et al. 2007), and  $(J-H) > 0.7$  (Zeidler et al. 2016). Right: CCD  $H-K_s$  vs.  $K_s-[4.5]$ . The black line marks the limit for the infrared selection with  $(H-K_s) < [(K_s-[4.5])-0.69] \times 0.98 + 0.3$ ,  $(H-K_s) > 0.65$  (Jose et al. 2016), and  $(K_s-[4.5]) > 0.49$ . Note that the selection criteria of Winston et al. (2007), and Jose et al. (2016) have been moved to the red by 0.2 magnitudes.

Gutermuth et al. (2009), with the CCD  $[K_s-[3.6]]_0$  versus  $[[3.6]-[4.5]]_0$  as shown in Figure 7. We obtained a total of 32 Class I YSOs and a total of 385 Class II YSOs.

Adding these sources to what was found in Phase I, the final result of the infrared color selection method for YSOs with disks is a total of 74 Class I YSOs and a total of 562 Class II YSOs.

## 5. X-Ray and Infrared Associations

### 5.1. Infrared Counterparts of the X-Ray Sources

We searched for near- and mid- infrared counterparts of the 249 detected X-ray sources in the VISTA/VVV and *Spitzer*/

GLIMPSE catalogs. In Figure 8, we show three-color VISTA and *Spitzer* images of the IRAS 16562-3959 region, on which we have superposed the position of the ACIS array. The astrometric registration between these catalogs is better than  $1''$ . Two different matching radii were used, because of the off-axis *Chandra* PSF degradation (Getman et al. 2005). We used  $1''$  for X-ray sources with off-axis position  $\theta \leq 3'$ , and the matching radius was enlarged to  $2''$  for  $\theta > 3'$ . When several counterparts of the same source were found, we chose the closest counterpart to the X-ray source. We found that 217 of the X-ray sources (87%) have near-infrared counterparts. We selected the  $J$ ,  $H$ , and  $K_s$  bands, and kept for the analysis only the sources



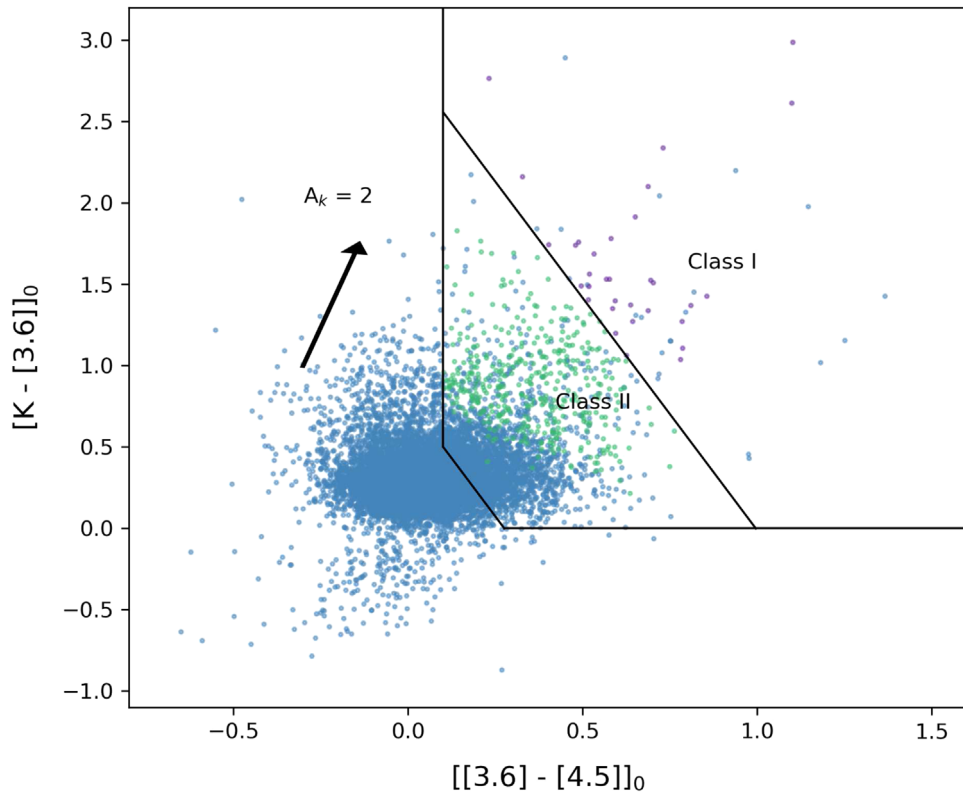


**Figure 7.** CCD  $[K - [3.6]]_0$  vs.  $[[3.6] - [4.5]]_0$  used for the isolation of Class I and Class II YSOs. Purple dots correspond to Class I YSOs, green dots correspond to Class II YSOs, and blue dots are field stars.

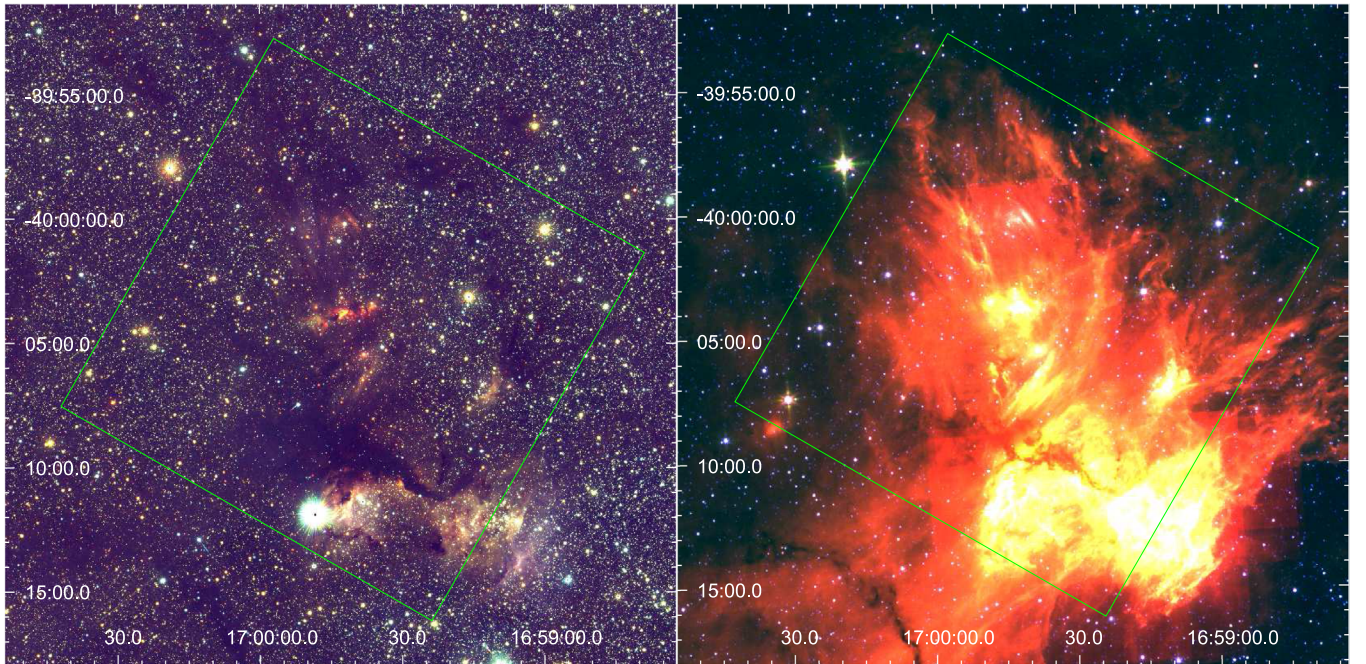


**Figure 8.** Left: VISTA/VVV survey three-color image with a  $J$ -,  $H$ -, and  $K_S$ -band composite of the IRAS 16562-3959 region. Right: *Spitzer*/GLIMPSE survey three-color image with  $[3.6]$ ,  $[5.8]$ , and  $[8.0]$  bands composite of the IRAS 16562-3959 region. The green square, for both images, indicates the position of the ACIS-I detector.

that have good detection in these three bands. We ended up with 165 counterparts, which corresponds to 66% of the X-ray sources. The sources and magnitudes are listed in Table 4. Similarly, we found that 151 of the X-ray sources (61%) have mid-infrared counterparts, which are listed with their

magnitudes on Table 4. We kept for the analysis all the mid-infrared counterparts having at least one good detection in one of the bands  $[3.6]$ ,  $[4.5]$ ,  $[5.8]$ , and  $[8.0] \mu\text{m}$ . The analysis of the X-ray counterparts in terms of determination of population class and contamination is detailed in Section 4 together with

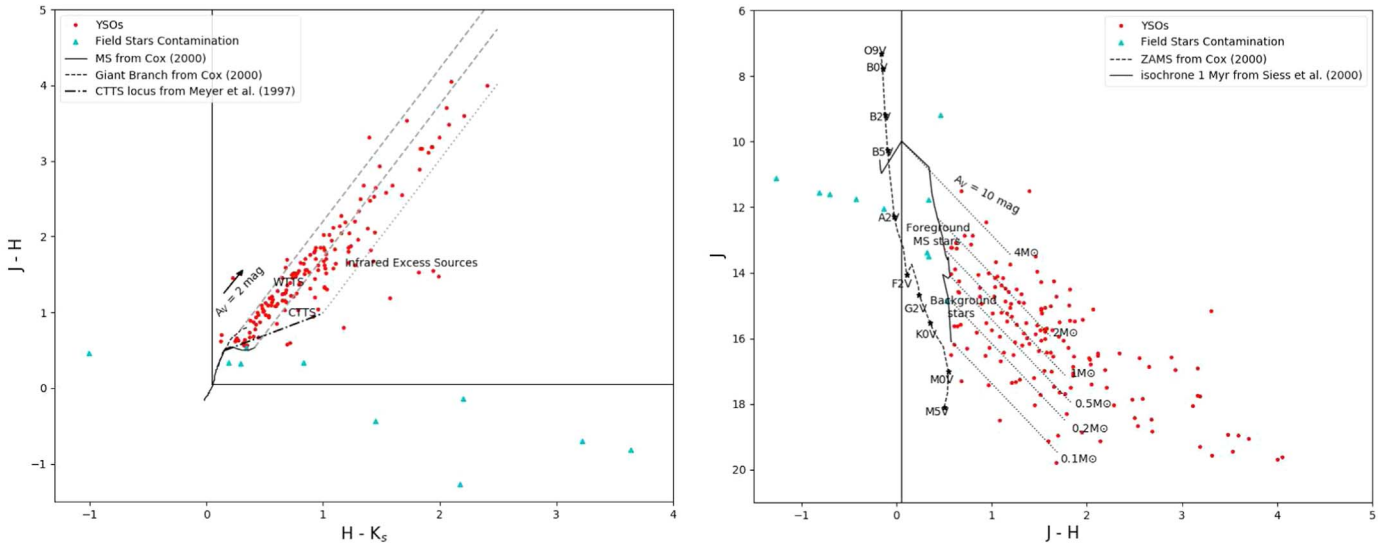


**Figure 9.** Left: CCD  $J-H$  vs.  $H-K_s$  of all X-ray sources having VISTA/VVV counterparts with high-quality photometry. The red dots correspond to YSOs, and the cyan triangles to contamination from field stars. The two straight black lines at  $(J-H) > 0.05$  mag and  $(H-K_s) > 0.05$  mag (Zeidler et al. 2016) mark the limit for the infrared selection. The solid and dashed black line mark the intrinsic color position for main-sequence and giant stars from Cox (2000). The gray dashed lines correspond to the reddening band for main-sequence stars from Rieke & Lebofsky (1985). The dashed-dotted line show the locus for CTTS from Meyer et al. (1997), and the dotted line marks the reddening band corresponding to the CTTS colors. Right: CMD  $J$  vs.  $J-H$  of the same stars as on the left panel. The straight black line at  $(J-H) > 0.05$  mag (Zeidler et al. 2016) marks the limit for the infrared selection. The dashed line indicates the location of the main-sequence stars at the distance to IRAS 16562-3959. The solid black line shows the 1 Myr isochrone from Siess et al. (2000). The dotted lines show the reddening vectors with  $A_V = 10$  mag for different stellar masses.

**Table 4**  
Infrared Counterparts

Source # (1)	$J$ (2)	$H$ (3)	$K_s$ (4)	[3.6] (5)	[4.5] (6)	[5.8] (7)	[8.0] (8)	Type (9)
1	...	...	...	...	...	...	...	Galactic contamination
2	...	$17.58 \pm 0.09$	$16.99 \pm 0.09$	...	...	...	...	Class III
3	$12.877 \pm 0.001$	$12.166 \pm 0.001$	$12.040 \pm 0.001$	$11.71 \pm 0.05$	$11.65 \pm 0.07$	$11.51 \pm 0.09$	...	Contamination
4	...	...	$17.61 \pm 0.16$	...	...	...	...	...
5	$14.244 \pm 0.003$	$13.584 \pm 0.003$	$13.324 \pm 0.004$	$13.03 \pm 0.07$	$13.32 \pm 0.11$	...	...	Contamination
6	...	...	...	...	...	...	...	AGN
7	...	...	...	...	...	...	...	Class II
8	$11.774 \pm 0.001$	$11.436 \pm 0.001$	$10.601 \pm 0.001$	$10.56 \pm 0.09$	$10.40 \pm 0.10$	$10.16 \pm 0.06$	$9.98 \pm 0.06$	Contamination
9	$14.942 \pm 0.004$	$14.049 \pm 0.004$	$13.670 \pm 0.005$	$13.20 \pm 0.07$	$13.22 \pm 0.10$	...	...	Class III
10	...	$16.38 \pm 0.03$	$14.13 \pm 0.01$	$12.23 \pm 0.08$	$11.69 \pm 0.09$	...	...	Field Star

(This table is available in its entirety in machine-readable form.)

the analysis of all infrared sources detected in the region. The results are presented in Table 4.

### 5.2. Selection of Class III YSOs

We used our X-ray-selected VISTA/VVV sources to identify Class III YSOs, by plotting the CCD  $J-H$  versus  $H-K_s$  shown in Figure 9. Sources defined as Class III YSOs or WTTS lack substantial warm inner disk material, and are thus considered diskless, but they still could exhibit transitional, or debris disks. They are located in the color space between the two gray dashed lines, where these sources do not exhibit any infrared excess, and thus can be explained by normal reddening. We found a total of 91 Class III YSOs. We also checked that the X-ray sources defined as Class II from the previous analysis are located in the color space defined by the reddened Classical T Tauri Star (CTTS, Class II) locus, and

that the Class I sources are located on the right side of the dotted line, corresponding to the Class I color space. We then proceeded to determine contamination using both CCD and the color-magnitude diagram (CMD)  $J$  versus  $J-H$  shown in Figure 9, where the sources considered as contamination from foreground and background stars (cyan triangles) are located to the left of the 1 Myr isochrone on the CMD, and below and on the left side of the main sequence on the CCD.

### 5.3. Unclassified X-Ray Sources

#### 5.3.1. X-Ray Sources without Infrared Counterpart

Of our detected X-ray sources, 32 lack infrared counterparts. We consider two reasons for this. The first one is that those sources are located in regions of high extinction and cannot be detected in the infrared. The second one is that those sources could be extragalactic contamination, in particular AGNs. We



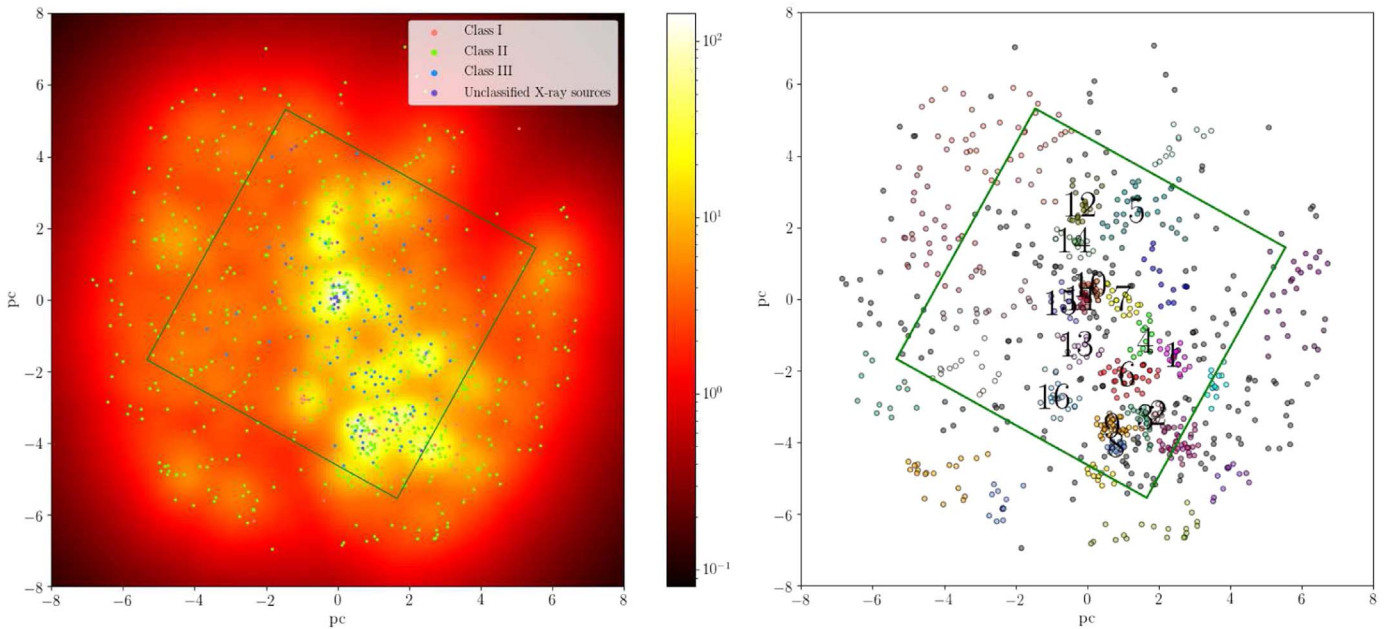


**Figure 10.** Left: surface density plot for all YSOs considered to be part of the region, with each dot corresponding to a source. Red dots correspond to Class I YSOs, green dots correspond to Class II, blue dots correspond to Class III, and purple dots correspond to unclassified X-ray sources. The units of the colors scale are number of sources per  $\text{pc}^2$ . The green square indicates the position of the ACIS-I detector. Right: clustering selection as determined with the HDBSCAN algorithm. The dots represent all YSOs considered to be part of the region, with each dot corresponding to a source. Each star cluster is represented with a different color. The clusters selected for further analysis are denoted by numbers.

consider sources that are located far from regions with high extinction or from the cluster, and that are very faint in X-ray, with count rates lower than 0.638 cts/ks, as possible AGN contamination. We also have three sources (sources 1, 226, and 248) that are located far from the cluster, but are very bright in X-rays. These sources are likely galactic contamination, such as X-ray binaries.

### 5.3.2. X-Ray Sources with Infrared Counterparts

We assume that the X-ray sources that have an incomplete set of infrared data are part of the cluster, and that the poor detection in the infrared is due to high extinction. Some of these sources have good detections in the H and  $K_S$  band only. A  $H-K_S$  color study of our Class II and Class III sources indicates that the  $H-K_S$  median for Class II sources is 1.27, and that for Class III sources it is 0.73. Therefore, we classify sources having  $H-K_S < 1$  as Class III, and sources having  $H-K_S > 1$  as Class II.

## 6. Subcluster Analysis

### 6.1. Subcluster Associations and Spatial Distribution

Inspecting the images at different wavelength bands (Figures 1 and 8), it is evident that the IRAS 16562-3959 region is not a simple centrally condensed cluster with the massive protostar at its center, but consist of several peak locations where stars have recently formed. In order to investigate the subcluster structure of the region, we have used the  $k$ th-nearest neighbor density estimator (kNN) (Casertano & Hut 1985), with  $k = 18$ , to obtain the YSO surface density. The result of this procedure is shown in Figure 10's left panel. We have overlaid on this figure the location of all YSOs as determined in the previous sections. YSO surface density enhancements with the presence of Class I–III YSOs are clearly detected, together with a more uniform distribution of Class II

objects. Note, however, that our YSO selection method is not sensitive to Class III object outside the ACIS field, i.e., on mid/near-IR data alone.

To further investigate the subcluster structure of IRAS 16562-3959, we used the hierarchical density-based clustering algorithm HDBSCAN (McInnes et al. 2017), which uses the kNN algorithm, in association with the minimum spanning tree from Prim's algorithm, and hierarchical cluster analysis, to determine the clustering in a data set (for more details see *How HDBSCAN Works*<sup>8</sup>). The resulting cluster selection from this algorithm is shown in Figure 10, right panel. While there appears to be clustering throughout the region, for further analysis we will concentrate on the clusters that match the YSO density enhancements in Figure 10 (left panel), with a threshold of 13 sources  $\text{pc}^{-2}$ . We thus selected 16 dense clusters, which we have labeled with numbers, from 1 to 16. In Table 5, we give the observed characteristics of each cluster, including the subcluster ID, the central position (the median position of all sources in the subcluster), the subcluster area using a convex hull algorithm that allows us to find the smallest polygon that contains a group of discrete points, the radius calculated from the convex hull area, the surface density for each subcluster, the total number of YSOs in each subcluster and their classification.

It is instructive to compare the subclusters in the IRAS 16562-3959 region with similar objects studied previously. While IRAS 16562-3959 clearly harbors a high-mass protostar that has already developed a luminosity approaching that of O-type ZAMS stars, the subclusters are generally smaller, and contain far less YSOs than similar high-mass star-forming young clusters, such as, for instance, the regions listed by Getman et al. (2014a). Also, the subcluster structures in these latter regions show a large variation in both size and number of stars compared to the subclusters we have defined

<sup>8</sup> [http://hdbscan.readthedocs.io/en/latest/how\\_hdbscan\\_works.html](http://hdbscan.readthedocs.io/en/latest/how_hdbscan_works.html)



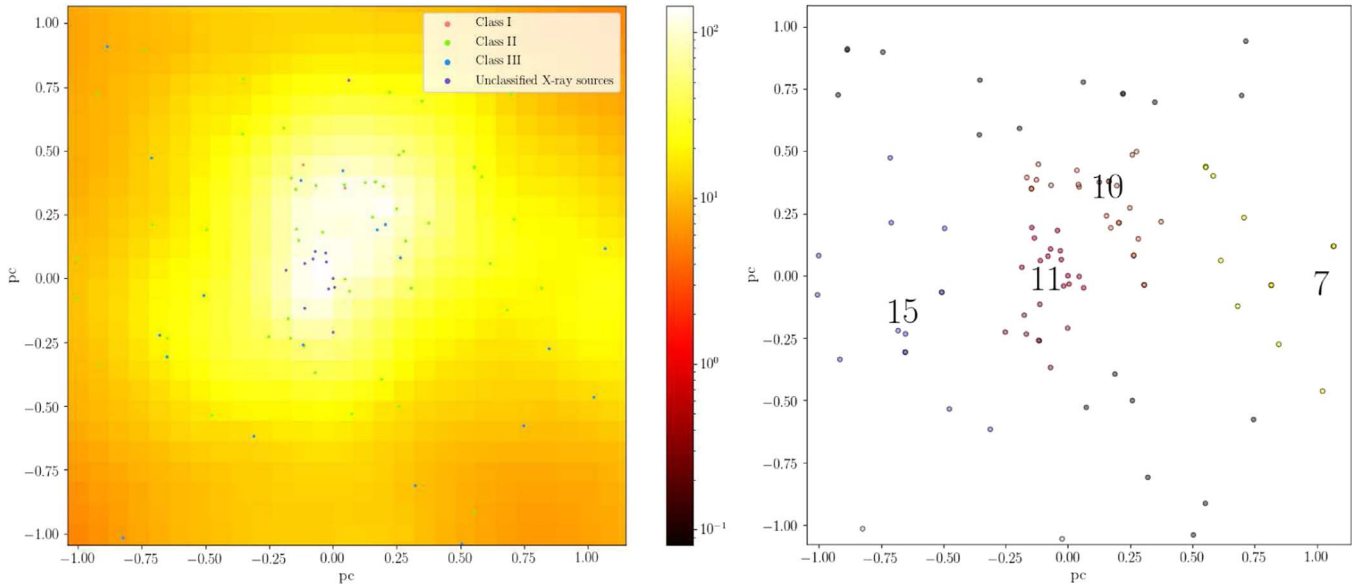


**Figure 11.** Left: close up of the central cluster from the surface density plot of Figure 10. Right: close up of the central cluster from the cluster membership plot of Figure 10.

**Table 5**  
Subcluster Structure Properties

Subcluster ID	R.A. (J2000)	Decl. (J2000)	$A_{\text{hull}}$ (pc $^2$ )	$R$ (pc)	$\sigma_{\text{hull}}$ (pc $^{-2}$ )	Total YSOs	Class I	Class II	Class III	Unclassified	Class II/Class I	Class III/Class II
(1)	(2)	(3)	(4)	(5)	(6)	(7)	(8)	(9)	(10)	(11)	(12)	(13)
1	16 <sup>h</sup> 59 <sup>m</sup> 13 <sup>s</sup> .41	-40 <sup>d</sup> 06 <sup>m</sup> 57 <sup>s</sup> .46	2.84	0.95	7.75	22	2	16	3	1	8.00	0.19
2	16 <sup>h</sup> 59 <sup>m</sup> 18 <sup>s</sup> .73	-40 <sup>d</sup> 10 <sup>m</sup> 13 <sup>s</sup> .18	1.19	0.62	10.08	12	1	8	3	0	8.00	0.38
3	16 <sup>h</sup> 59 <sup>m</sup> 22 <sup>s</sup> .96	-40 <sup>d</sup> 10 <sup>m</sup> 29 <sup>s</sup> .87	2.94	0.97	7.48	22	3	14	3	2	4.67	0.21
4	16 <sup>h</sup> 59 <sup>m</sup> 23 <sup>s</sup> .20	-40 <sup>d</sup> 06 <sup>m</sup> 07 <sup>s</sup> .87	2.88	0.96	4.51	13	0	5	6	2	$\infty$	1.20
5	16 <sup>h</sup> 59 <sup>m</sup> 25 <sup>s</sup> .60	-39 <sup>d</sup> 58 <sup>m</sup> 48 <sup>s</sup> .32	7.18	1.51	4.87	35	5	23	5	2	4.60	0.22
6	16 <sup>h</sup> 59 <sup>m</sup> 28 <sup>s</sup> .61	-40 <sup>d</sup> 08 <sup>m</sup> 04 <sup>s</sup> .14	4.10	1.14	7.31	30	1	14	12	3	14.00	0.86
7	16 <sup>h</sup> 59 <sup>m</sup> 29 <sup>s</sup> .99	-40 <sup>d</sup> 03 <sup>m</sup> 48 <sup>s</sup> .29	2.78	0.94	6.83	19	0	14	5	0	$\infty$	0.36
8	16 <sup>h</sup> 59 <sup>m</sup> 32 <sup>s</sup> .12	-40 <sup>d</sup> 12 <sup>m</sup> 05 <sup>s</sup> .50	1.28	0.64	12.48	16	0	14	1	1	$\infty$	0.07
9	16 <sup>h</sup> 59 <sup>m</sup> 33 <sup>s</sup> .52	-40 <sup>d</sup> 11 <sup>m</sup> 00 <sup>s</sup> .22	3.12	1.00	11.55	36	6	20	5	5	3.33	0.25
10	16 <sup>h</sup> 59 <sup>m</sup> 39 <sup>s</sup> .70	-40 <sup>d</sup> 03 <sup>m</sup> 00 <sup>s</sup> .77	1.67	0.73	15.53	26	4	17	5	0	4.25	0.29
11	16 <sup>h</sup> 59 <sup>m</sup> 42 <sup>s</sup> .47	-40 <sup>d</sup> 03 <sup>m</sup> 45 <sup>s</sup> .88	1.37	0.66	16.09	22	0	10	1	11	$\infty$	0.10
12	16 <sup>h</sup> 59 <sup>m</sup> 42 <sup>s</sup> .89	-39 <sup>d</sup> 58 <sup>m</sup> 27 <sup>s</sup> .69	3.63	1.08	6.05	22	5	16	1	0	3.20	0.06
13	16 <sup>h</sup> 59 <sup>m</sup> 44 <sup>s</sup> .09	-40 <sup>d</sup> 06 <sup>m</sup> 23 <sup>s</sup> .44	3.34	1.03	5.08	17	5	8	4	0	1.60	0.50
14	16 <sup>h</sup> 59 <sup>m</sup> 45 <sup>s</sup> .07	-40 <sup>d</sup> 00 <sup>m</sup> 30 <sup>s</sup> .35	2.84	0.95	7.40	21	2	15	3	1	7.50	0.20
15	16 <sup>h</sup> 59 <sup>m</sup> 49 <sup>s</sup> .04	-40 <sup>d</sup> 04 <sup>m</sup> 01 <sup>s</sup> .69	2.77	0.94	5.06	14	0	9	5	0	$\infty$	0.56
16	16 <sup>h</sup> 59 <sup>m</sup> 51 <sup>s</sup> .38	-40 <sup>d</sup> 09 <sup>m</sup> 20 <sup>s</sup> .82	3.79	1.10	5.28	20	11	8	1	0	0.73	0.13

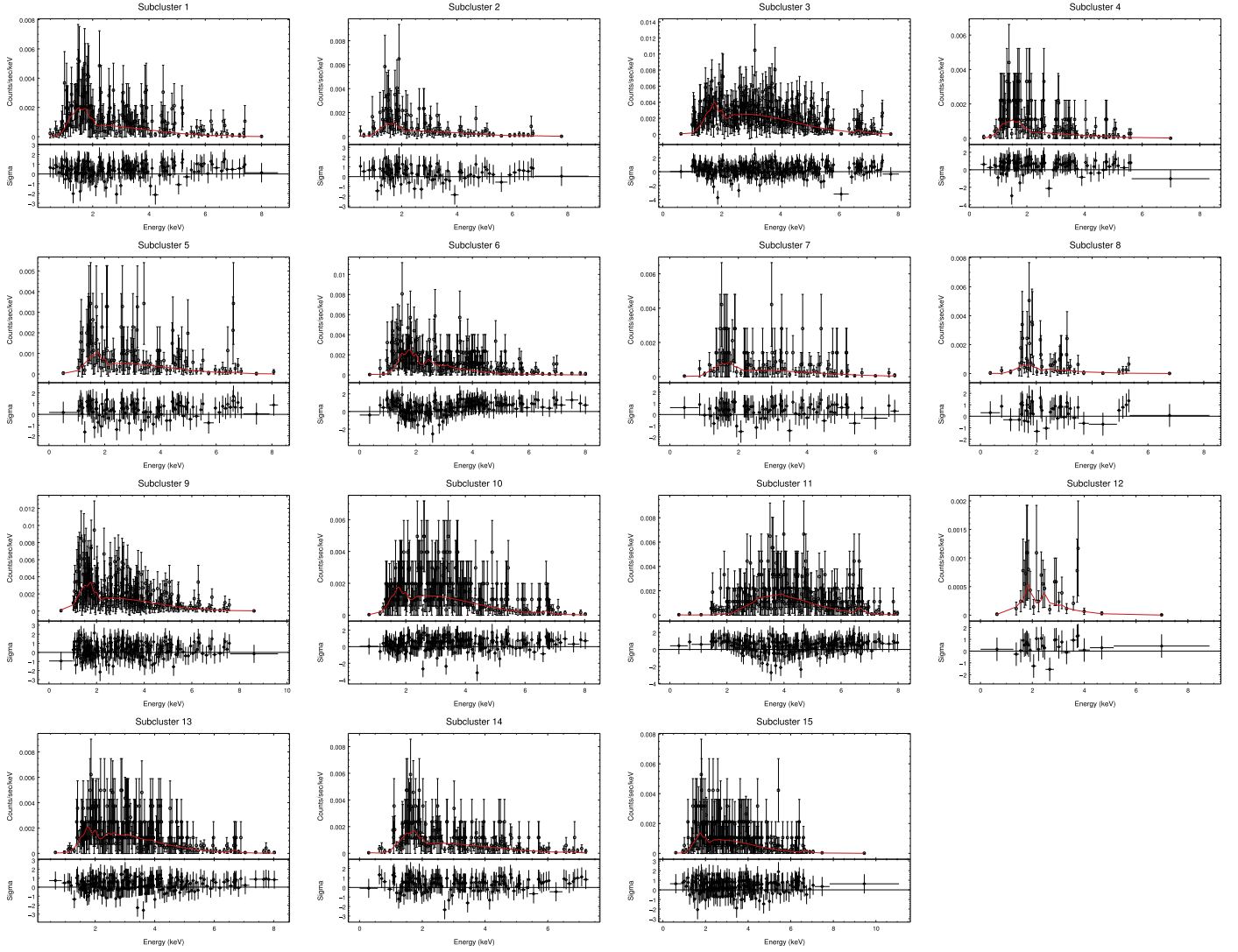
above, which are much more uniform in appearance. Our subclusters appear much more similar to the clusters studied by Gutermuth et al. (2009), in terms of physical size, and number of YSOs, and hence also in terms of YSO surface densities. Furthermore, the ratio of the number of Class II and Class I YSOs is similar. Most of the brightest sources in the clusters studied by Gutermuth et al. (2009) have IRAS luminosities below  $10^4 L_{\odot}$ , indicating that no massive stars are present.

It is further important to point out that the high-mass protostar in IRAS 16562-3959 is located in subcluster 11, which has the highest observed YSO surface density, as shown in Figure 11. We determined a population of 22 YSOs, including the high-mass protostar, of which 91% were detected in X-rays, and 60% of these X-ray sources have VISTA near-infrared counterparts. Subcluster 11 has the largest fraction of

X-ray sources which were not detected at near- and mid-infrared wavelengths, and thus the most unclassified sources due to extinction. Clearly, the surface density associated with the high-mass protostar, as derived from the IR analysis, needs to be regarded as a lower limit.

## 6.2. Subcluster X-Ray Emission

We have also measured the average X-ray emission per star in each subcluster. This was done for subclusters containing at least two X-ray sources. We added all counts in each subcluster region, and divided by the sum of the exposure times to derive an average count rate spectrum. These data are shown in Figure 12. Subsequently, we used the same technique to fit the average X-ray spectrum for each subcluster with a thermal

**Figure 12.** Fitted average X-ray spectra for each subcluster.**Table 6**  
Subcluster Average X-Ray Properties

Subcluster	$N_H$ $10^{22} \text{ (cm}^{-2}\text{)}$	kT (keV)	EM $10^{-5} \text{ (cm}^{-3}\text{)}$	$F_{x,c}$ $10^{-14} \text{ (erg cm}^{-2} \text{ s}^{-1}\text{)}$	$\log L_{x,c}$ $\text{(erg s}^{-1}\text{)}$	Reduced $\chi^2$
(1)	(2)	(3)	(4)	(5)	(6)	(7)
1	$0.70^{+0.27}_{-0.22}$	5.53	$1.07^{+0.20}_{-0.18}$	$1.53^{+0.27}_{-0.28}$	30.72	0.70
2	$0.82^{+0.38}_{-0.31}$	6.84	$1.15^{+0.28}_{-0.26}$	$1.72^{+0.41}_{-0.41}$	30.77	0.69
3	$2.08^{+0.32}_{-0.28}$	5.97	$3.38^{+0.37}_{-0.35}$	$4.92^{+0.52}_{-0.54}$	31.23	0.81
4	$0.49^{+0.31}_{-0.23}$	4.32	$0.41^{+0.11}_{-0.10}$	$0.54^{+0.14}_{-0.14}$	30.27	0.74
5	$1.33^{+0.55}_{-0.43}$	6.48	$0.70^{+0.17}_{-0.16}$	$1.03^{+0.24}_{-0.25}$	30.55	0.68
6	$2.38^{+0.61}_{-0.46}$	1.50	$2.12^{+0.60}_{-0.47}$	$1.94^{+0.51}_{-0.50}$	30.83	0.78
7	$1.14^{+0.52}_{-0.37}$	6.85	$0.55^{+0.14}_{-0.13}$	$0.83^{+0.20}_{-0.22}$	30.46	0.55
8	$1.76^{+1.21}_{-0.75}$	1.72	$1.72^{+1.14}_{-0.83}$	$1.59^{+0.90}_{-0.86}$	30.74	0.72
9	$0.94^{+0.26}_{-0.21}$	13.29	$1.10^{+0.16}_{-0.15}$	$1.74^{+0.26}_{-0.26}$	30.78	0.73
10	$2.60^{+0.38}_{-0.31}$	3.83	$1.75^{+0.23}_{-0.22}$	$2.23^{+0.27}_{-0.29}$	30.89	0.67
11	$13.29^{+3.25}_{-2.61}$	2.00	$7.93^{+2.32}_{-1.83}$	$7.67^{+1.89}_{-2.17}$	31.42	0.76
12	$4.10^{+1.64}_{-1.03}$	0.89	$10.93^{+7.03}_{-4.73}$	$12.52^{+6.78}_{-6.46}$	31.64	0.64
13	$3.08^{+0.42}_{-0.35}$	2.48	$4.18^{+0.60}_{-0.56}$	$4.41^{+0.61}_{-0.64}$	31.18	0.57
14	$1.24^{+0.31}_{-0.25}$	5.19	$0.79^{+0.13}_{-0.13}$	$1.10^{+0.19}_{-0.20}$	30.58	0.60
15	$2.48^{+0.45}_{-0.37}$	3.65	$1.80^{+0.29}_{-0.27}$	$2.24^{+0.31}_{-0.35}$	30.89	0.60

**Table 7**  
Age and Disk Fraction Estimates for Each Subcluster

Subcluster	$N_{\text{tot}}$	$N_{\text{Age}}$	Median ( $J-H$ )	Median Age (Myr)	$N_{\text{disk}}$	$N_{\text{diskless}}$	$N_{\text{diskfrac}}$	Disk Fraction
(1)	(2)	(3)	(4)	(5)	(6)	(7)	(8)	(9)
1	22	6	1.26	$1.84^{+1.67}_{-0.84}$	18	3	21	0.86
2	12	3	1.22	$1.91^{+1.79}_{-0.81}$	9	3	12	0.75
3	22	6	1.68	$1.12^{+1.13}_{-0.37}$	17	3	20	0.85
4	13	7	1.16	$2.02^{+1.68}_{-0.82}$	5	6	11	0.45
5	35	5	1.01	$2.27^{+1.78}_{-1.02}$	28	5	33	0.85
6	30	13	1.26	$1.85^{+1.69}_{-0.86}$	15	12	27	0.56
7	19	7	1.58	$1.30^{+1.25}_{-0.50}$	14	5	19	0.74
8	16	1	1.66	$1.16^{+1.22}_{-0.41}$	14	1	15	0.93
9	36	8	1.72	$1.08^{+1.12}_{-0.38}$	26	5	31	0.84
10	26	11	1.87	$1.02^{+1.03}_{-0.32}$	21	5	26	0.81
11	22	7	2.54	$0.75^{+0.83}_{-0.27}$	10	1	11	0.91
12	22	2	2.40	$0.81^{+0.89}_{-0.31}$	21	1	22	0.95
13	17	8	1.58	$1.30^{+1.25}_{-0.50}$	13	4	17	0.76
14	21	8	1.94	$0.99^{+1.01}_{-0.32}$	17	3	20	0.85
15	14	6	2.22	$0.88^{+0.84}_{-0.33}$	9	5	14	0.64
16	20	1	1.13	$2.07^{+1.98}_{-0.92}$	19	1	20	0.95

**Note.** (1) Cluster designation. (2) Total number of YSOs in each cluster. (3) Number of YSOs having near-infrared counterparts used for the age calculation. (4) Median color ( $J-H$ ) for all stars having near-infrared counterparts in each cluster. (5) Median age calculated for all stars having near-infrared counterparts in each cluster. The uncertainties are the 25% and 75% quartiles of the  $\text{Age}_{JX}$  versus  $J-H$  distribution from Getman et al. (2014a). (6) Number of YSOs with disks (Class I and Class II). (7) Number of YSOs without disks (Class III). (8) Number of YSOs used for the disk fraction calculation. (9) Disk fraction calculated for each cluster; see the text for more details.

spectrum plus one absorption component as described in the Section 3.3. The results of the fits are listed in Table 6.

### 6.3. Age Estimation

In order to estimate the age of each subcluster, we used the  $\text{Age}_{JX}$  method described in Getman et al. (2014a). Specifically, we use Equations (1) and (2) of that paper to calculate the median age of each subcluster based on its median  $J-H$  value. In Table 7 we list for each subcluster (column 1), the number of stars (column 2), the number of stars used in the median age calculation (column 3), the median  $J-H$  values (column 4), and the median ages for each subcluster (column 5). The derived ages range between 0.75 Myr (subcluster 11) to 2.27 Myr (subcluster 5). We also calculated the disk fraction in each subcluster as follows: Disk Fraction =  $\frac{N_{\text{disk}}}{(N_{\text{disk}} + N_{\text{diskless}})}$ , with  $N_{\text{disk}}$  being the number of YSOs with disks (Class I and Class II), and  $N_{\text{diskless}}$  the number of YSOs without disks (Class III). In Table 7, we list the number of stars used in the disk fraction calculation (column 6), the number of stars with and without disks (columns 7 and 8, respectively), and in column 9 the disk fraction.

## 7. Discussion

In this study we have attempted to characterize the stellar population in IRAS 16562-3959, with emphasis on the environment of the high-mass protostar located in this region. Inspecting Figure 8, it is clear that IRAS 16562-3959 is located within a much larger region of projected size  $\geq 10$  pc, and the presence of many young stars in this area indicates that star formation has taken place throughout the region. Furthermore, being located at the northern end of the Sco OB1 association, there are several young clusters and H II regions toward the southwest of IRAS 16562-3959, demonstrating that high-mass

star formation has occurred over a large spatial scale. Recently, Damiani (2018) reported evidence of a sequence of star formation in the Sco OB1 association from south to north. Given that there are fully formed high-mass stars located at 2.5 pc to the southwest of a high-mass protostar, one might ask whether triggered star formation is also evident in the much smaller region covered in our *Chandra* observations. Considering, however, the median ages of our subclusters, we see that there is no clear age gradient. For instance, while subcluster 11, which contains the high-mass protostar, has in fact the youngest median age (0.75 Myr), the oldest subcluster 5 (2.27 Myr) is located on the opposite side of subcluster 11. Thus, while the high-mass star formation to the southwest could have influenced and perhaps induced star formation in the region, a clear propagation direction is not evident in the median age distribution.

The estimates of the ages for the identified subclusters in the region allow us to investigate a number of issues in the star formation history of the region. First, the X-ray analysis presented in this and many similar works profits from the fact that young stars are far more X-ray luminous than main-sequence stars. The evolution toward lower X-ray luminosities with time is nicely documented in Figure 4 of Preibisch & Neuhäuser (1995), which shows a decrease of median X-ray luminosity from about  $10^{30.5} \text{ erg s}^{-1}$  for young clusters to  $10^{27.5} \text{ erg s}^{-1}$  for main-sequence field stars within a time period of 4 Myr. We have checked in our data set if this trend is also present in the subclusters associated with the IRAS 16562-3959 region, by looking at the average X-ray luminosity of each cluster versus median age. While there is a large scatter, a trend of decreasing X-ray luminosity with age is evident. Second, many studies have attempted to use the disk fraction determined from NIR photometry as an age indicator (e.g., Haisch et al. 2001). However, there appears to be a large spread



of ages for disk lifetimes (e.g., Hernández et al. 2008), for a variety of reasons, partly due to observational limitations, and partly due to environmental influences within the star-forming clusters. Hence, considering our data of the disk fraction versus age, it appears that the disk fraction of our subclusters is uniformly distributed with median age, and therefore, we do not detect a clear correlation. Third, our data allow us to check whether the clusters' stars are unbound, and that the cluster is hence expanding. By looking at the stellar surface density versus the age of the subcluster, we again observe a decreasing trend in the surface density with median age. In particular, our youngest subcluster 11, which contains the high-mass protostar, has the highest surface density.

We will now turn to the immediate surroundings of the high-mass protostar G345.4938+01.4677. It is located in subcluster 11, which is the youngest and most deeply embedded subcluster in this region. As pointed out above, it also has the highest surface density of young stellar objects, which due to the large extinction toward this subcluster of  $N_H \approx 10^{23} \text{ cm}^{-2}$ , is only a lower limit. We have detected an X-ray source (source # 161) coincident with the peak of radio continuum emission, which is presumably the position of the high-mass protostar. This emission will be discussed in more detail in a future paper. The position of this object is coincident with the (0,0) position in Figures 10 and 11, and from inspection of Figure 11, it is evident that the high-mass protostar is located near the center of subcluster 11. Surrounding subcluster 11 are subclusters 7, 10, and 15. We note that these three subclusters have median ages from 0.9 to 1.3 Myr, and all have lower surface densities than subcluster 11. We thus find that the high-mass protostar is embedded in a dense cluster, and surrounded with a less dense and older distribution of stars, i.e., the stellar distribution can be described as a core-halo structure with an inside-out age gradient.

This result adds to recent findings of a similar nature. For instance, a core-halo structure is evident in several clusters studied by Gutermuth et al. (2009), and recently Getman et al. (2014b) reported core-halo age gradients in Orion and NGC 2024. The recent papers by Rivilla et al. (2013) on Orion and DR21 show similar results: in Orion, the most massive star  $\theta^1$  Ori C is surrounded by a ring of non-extincted (i.e., likely more evolved) PMS low-mass stars, and in DR21, they found evidence for mass, and age segregation, with the youngest stars still embedded in the N-S cloud, and more evolved stars more spatially distributed. Another example is the study of IRAS 19343 + 2024 by Ojha et al. (2010): a high-mass protostellar cluster composed of at least four early B-type stars (age  $\sim 10^4$ – $10^5$  yr) surrounded by a rich population of low-mass stars with ages 1–3 Myr. While Getman et al. (2014b) discussed a number of possible scenarios to explain the observed age gradient and core-halo structure, the data presented in our study appear to favor the competitive accretion theory for high-mass star formation, where massive stars are expected to form later than the low-mass stars in the cluster (Tan et al. 2014).

Finally, it is worthwhile to consider our observational results with reference to a possible observational bias, which could influence the judgment of whether the monolithic core accretion scenario of McKee & Tan (2003), or the competitive accretion scenario of Bonnell et al. (2001) is more applicable to the formation of high-mass stars. Candidates for high-mass protostars like the one studied in this paper are often found by deep interferometric radio continuum surveys toward regions

of high-FIR luminosity, or massive molecular or dust cores. Because such observations are generally dynamic range limited, targets are often chosen from fields, which are very radio-quiet (e.g., Rosero et al. 2016), i.e., regions which are void of signs of previous high-mass star formation in the form of ultra-compact or hyper-compact H II regions. In fact, radio observations of IRAS 16562-3959 show no other detection of radio continuum sources, and hence possible high-mass (proto) stars at very low limits ( $\mu\text{Jy}$ ) within 2 pc (Guzmán et al. 2016, V.A. Montes et al. 2019, in preparation). The early B-type protostar in IRAS 20126+4104 is a similar example (e.g., Hofner et al. 2007). Hence, one might think that this selection method would bias against star formation theories that invoke stellar clusters, and bias toward high-mass stars that might form in isolation. However, the present and other studies (e.g., Montes et al. 2015) demonstrate that also in objects selected in this fashion, an older low-mass stellar cluster is present, indicating that the high-mass protostar may have been the last one to form in the cluster.

## 8. Summary

We have performed a combined X-ray/infrared study of the young stellar population associated with the high-mass protostellar candidate in IRAS 16562-3959. The main results of this study are:

(1) We detected 249 X-ray sources within the *Chandra* ACIS-I field of view. 70% of them have a count rate lower than 0.638 cts/ks. The majority of the sources have a hard X-ray spectrum. We were able to obtain meaningful spectral fit results for 98 sources. The fitted  $N_H$  values range from  $2.1 \times 10^{21} \text{ cm}^{-2}$  to  $4.1 \times 10^{23} \text{ cm}^{-2}$ , and the corrected luminosities from  $3.9 \times 10^{30} \text{ erg s}^{-1}$  to  $7.4 \times 10^{32} \text{ erg s}^{-1}$ , meaning that only relatively luminous X-ray sources were detected.

(2) Phase I of the infrared analysis, using only the *Spitzer*/GLIMPSE data, resulted in the identification of 218 YSOs, with 42 Class I, and 177 Class II YSOs. Phase II of the infrared analysis, combining *Spitzer*/GLIMPSE and VISTA/VVV data, yielded 417 YSOs, with 32 Class I, and 385 Class II YSOs. Combining the results from Phase I and Phase II, it was found that a total of 636 YSOs are associated with the region, with 74 Class I and 562 Class II YSOs.

(3) We found that 87% of the X-ray detections (217 sources) have near-infrared counterparts, but only 66% (165 sources) have good detections in the *J*, *H*, and *K<sub>s</sub>* bands. We also found that 61% of the X-ray detections (151 sources) have mid-infrared counterparts. The X-ray/infrared analysis resulted in the identification of 91 Class III YSOs. Combining the results of the X-ray/infrared analysis, with the results of the infrared analysis, we conclude that we have a total of 727 YSOs associated with the region, with 74 Class I, 562 Class II, and 91 Class III YSOs.

(4) We found that the region is composed of 16 subclusters. We observed a decreasing trend in the average X-ray luminosity with age, no clear correlation between disk fraction and age, and a decreasing trend in the surface density with age. Also, triggered star formation is not evident in the region.

(5) In the vicinity of the high-mass protostar, the stellar distribution has a core-halo structure. The subcluster in which the high-mass protostar was formed appears to be the youngest and has the highest surface density. The high-mass protostar (age  $\sim 10^5$  yr), in its subcluster, is surrounded by older low-mass pre-main sequence stars (age  $\sim 10^6$  yr), and it is located at the

center. The results of the study are compatible with the competitive accretion model of Bonnell et al. (2001).

P.H. acknowledges support from SAO grants GO3-14005X and GO5-16008X, as well as partial support from NSF grants AST-0908901 and AST-1814011 for this work. We thank the New Mexico Institute of Mining and Technology Research Office for their support. We also thank the anonymous referee for comments that improved this manuscript.

### ORCID iDs

Virginie A. Montes  <https://orcid.org/0000-0001-6538-3936>

### References

- Benjamin, R. A., Churchwell, E., Babler, B. L., et al. 2003, *PASP*, **115**, 953
- Bonnell, I. A., Clarke, C. J., Bate, M. R., & Pringle, J. E. 2001, *MNRAS*, **324**, 573
- Casertano, S., & Hut, P. 1985, *ApJ*, **298**, 80
- Cesaroni, R., Felli, M., Churchwell, E., & Walmsley, M. 2005, in IAU Symp. 227, *Massive Star Birth: A Crossroads of Astrophysics* (Cambridge: Cambridge Univ. Press)
- Chen, B. Q., Schultheis, M., Jiang, B. W., et al. 2013, *A&A*, **550**, A42
- Cox, A. N. 2000, *Allen's Astrophysical Quantities* (4th ed.; New York: Springer)
- Damiani, F. 2018, *A&A*, **615**, A148
- de Wit, W. J., Testi, L., Palla, F., & Zinnecker, H. 2005, *A&A*, **437**, 247
- Feigelson, E. D., & Montmerle, T. 1999, *ARA&A*, **37**, 363
- Flaccomio, E., Micela, G., & Sciortino, S. 2012, *A&A*, **548**, A85
- Freeman, P. E., Kashyap, V., Rosner, R., & Lamb, D. Q. 2002, *ApJS*, **138**, 185
- Fridriksson, J. K., Homan, J., Lewin, W. H. G., Kong, A. K. H., & Pooley, D. 2008, *ApJS*, **177**, 465
- Garmire, G., Bautz, M. W., Ford, P. G., Nousek, J. A., & Ricker, G. R. 2003, *Proc. SPIE*, **4851**, 28
- Getman, K. V., Feigelson, E. D., Grosso, N., et al. 2005, *ApJS*, **160**, 353
- Getman, K. V., Feigelson, E. D., Kuhn, M. A., et al. 2014a, *ApJ*, **787**, 108
- Getman, K. V., Feigelson, E. D., & Kuhn, M. A. 2014b, *ApJ*, **787**, 109
- Gregory, P. C., & Lored, T. J. 1992, *ApJ*, **398**, 146
- Grosso, N., Montmerle, T., Feigelson, E. D., et al. 1997, *Natur*, **387**, 56
- Gutermuth, R. A., Megeath, S. T., Myers, P. C., et al. 2009, *ApJS*, **184**, 18
- Guzmán, A. E., Garay, G., & Brooks, K. J. 2010, *ApJ*, **725**, 734
- Guzmán, A. E., Garay, G., Rodríguez, L. F., et al. 2014, *ApJ*, **796**, 117
- Guzmán, A. E., Garay, G., Rodríguez, L. F., et al. 2016, *ApJ*, **826**, 208
- Haisch, K. E., Lada, E. A., & Lada, C. J. 2001, *ApJL*, **553**, L153
- Hernández, J. A., Hartmann, L., Calvet, N., et al. 2008, *ApJ*, **686**, 1195
- Hofner, P., Cesaroni, R., Olmi, L., et al. 2007, *A&A*, **465**, 197
- Hofner, P., Delgado, H., Whitney, B., Churchwell, E., & Linz, H. 2002, *ApJ*, **579**, 95
- Imanishi, K., Koyama, K., & Tsuboi, Y. 2001, *ApJ*, **557**, 747
- Jose, J., Kim, J. S., Herczeg, G. J., et al. 2016, *ApJ*, **822**, 49
- Kennicutt, R. C. 1998, *ARA&A*, **36**, 189
- Lada, C. J., & Lada, E. A. 2003, *ARA&A*, **41**, 57
- López, C., Bronfman, L., May, J., Nyman, L.-A., & Garay, G. 2011, *A&A*, **534**, A131
- López-Calderon, C., Bronfman, L., Nyman, L.-A., et al. 2016, *A&A*, **595**, A88
- McInnes, L., Healy, J., & Astels, S. 2017, *JOSS*, **2**, 205
- McKee, C. F., & Tan, J. C. 2003, *ApJ*, **585**, 850
- Megeath, S. T., Gutermuth, R., Muzerolle, J., et al. 2012, *AJ*, **144**, 192
- Meyer, M. R., Calvet, N., & Hillenbrand, L. A. 1997, *AJ*, **114**, 288
- Minniti, D., Lucas, P. W., Emerson, J. P., et al. 2010, *NewA*, **15**, 433
- Montes, V. A., Hofner, P., Anderson, C., & Rosero, V. 2015, *ApJS*, **219**, 41
- Neuhäuser, R., & Preibisch, T. 1997, *A&A*, **322**, L37
- Ojha, D. K., Kumar, M. S. N., Davis, C. J., & Grave, J. M. C. 2010, *MNRAS*, **407**, 1807
- Oskinova, L. M., Steinke, M., Hamann, W.-R., et al. 2013, *MNRAS*, **436**, 3357
- Preibisch, T., & Neuhäuser, R. 1995, in *Lecture Notes in Physics, Properties of X-ray Flares on Young Stars, Flares and Flashes*, Vol. 454 ed. J. Greiner, H. W. Duerbeck, & R. E. Gershberg (Berlin, Heidelberg: Springer)
- Rieke, G. H., & Lebofsky, M. J. 1985, *ApJ*, **288**, 618
- Rivilla, V. M., Martín-Pintado, J., Jiménez-Serra, I., & Rodríguez-Franco, A. 2013, *A&A*, **554**, A48
- Rosero, V., Hofner, P., Claussen, M., et al. 2016, *ApJS*, **227**, 25
- Rots, A. H. 2006, in ASP Conf. 351, *adass XV*, ed. C. Gabriel (San Francisco, CA: ASP), 73
- Siess, L., Dufour, E., & Forestini, M. 2000, *A&A*, **358**, 593
- Soto, M., Barbá, R., Gunthardt, G., et al. 2013, *A&A*, **552**, A101
- Tan, J. C., Beltrán, M. T., Caselli, P., et al. 2014, in *Protostars and Planets VI*, ed. H. Beuther et al. (Tucson, AZ: Univ. Arizona Press), 149
- Townsend, L. K., Broos, P. S., Garmire, G. P., et al. 2014, *ApJS*, **213**, 1
- Weisskopf, M. C., Brinkman, B., Canizares, C., et al. 2002, *PASP*, **114**, 1
- Weisskopf, M. C., O'Dell, S., & Van Speybroeck, L. P. 1996, *Proc. SPIE*, **2805**, 2
- Winston, E., Megeath, S. T., Wolk, S. J., et al. 2007, *ApJ*, **669**, 493
- Winston, E., Wolk, S. J., Bourke, T. L., et al. 2011, *ApJ*, **743**, 166
- Zeidler, P., Preibisch, T., Ratzka, T., Roccatagliata, V., & Petr-Gotzens, M. G. 2016, *A&A*, **585**, A49